11th International Symposium on Turbulence and Shear Flow Phenomena (TSFP11)
Southampton, UK, July 30 to August 2, 2019

COHERENT-VORTICITY PRESERVING LARGE-EDDY SIMULATION (CVP-LES) OF TOPOLOGICALLY COMPLEX VORTICES

Zongxin Yu
School of Mechanical Engineering
Purdue University
West Lafayette, Indiana, USA
yu754@purdue.edu

Jean-Baptiste Chapelier
School of Mechanical Engineering
Purdue University
West Lafayette, Indiana, USA
jchapeli@purdue.edu

Carlo Scalo
School of Mechanical Engineering
Purdue University
West Lafayette, Indiana, USA
scalo@purdue.edu

ABSTRACT

This paper presents a novel dynamic Large-Eddy Simulation methodology, termed Coherent-vorticity Preserving, or CvP (Chapelier *et al.*, 2018), which relies on an enstrophy-based eddy-viscosity correction that removes excessive subgrid dissipation in areas of the flow that are well resolved by the grid and/or with negligible turbulent fluctuation levels. CvP-LES has been successfully applied to homogeneous isotropic turbulence, wall-bounded flows (Chapelier *et al.*, 2018), helical vortices (Chapelier *et al.*, 2019), and vortex rings (Yu *et al.*, 2018*b*).

In this manuscript we focus on recent advancements made in the application of CvP-LES to topologically complex vortex knots, focusing on: (1) reconnection mechanisms at moderately high Reynolds numbers ($Re_\Gamma = 2 \times 10^4$) of a trefoil knot-shaped vortex, inspired by the experiments of Kleckner & Irvine (2013), and (2) the dynamics of formation of *axial flow*, generated during the reconnection in the same setup. Axial flow is defined as flow velocity oriented along the main direction of the vorticity vector; as such, it yields a non-zero helicity. From the CvP-LES calculations we in fact extract the probability density functions of helicity during and after the reconnection event, demonstrating the correlation of the axial flow with high helicity fluctuations and its role in vortex bursting. This paper also features a validation of the CvP methodology against experimental data and low-Reynolds number simulations, emphasizing the high-fidelity of the present numerical methodology for the representation of complex vortex reconnection mechanisms.

INTRODUCTION

Viscous reconnection of vortices has raised a strong interest in the fluid mechanics community for over several decades. This fundamental process occurs in a variety of flow configurations including the reconnection of large-scale aircraft wake vortices reviewed by Spalart (1998), the interaction of vortices shed from helicopter rotor blades, or fine-scale mixing in turbulence studied by Hussain (1986).

The knotted vortex configuration is of particular interest, as they feature viscous reconnection involving both anti-parallel and orthogonal vortex tubes (Kida & Takaoka, 1987; Kleckner & Irvine, 2013; Scheeler *et al.*, 2014; Kimura & Moffatt, 2014). This vortex system also provides an interesting framework for the study of the propagation of Kelvin waves and axial flow along the vortex tubes that are generated as a consequence of the reconnection process.

The present study introduces Large-Eddy simulations of the dynamics of knotted vortices at a moderately high Reynolds number, using the CvP-LES approach introduced by Chapelier *et al.* (2018), which has been found successful to predict the transition and turbulent breakdown of temporally developing helical vortices (Chapelier *et al.*, 2019). A circulation Reynolds number of $Re_\Gamma = 20,000$ is considered, made computationally feasible by the CvP-LES methodology. Additional computations have been performed in a separated work currently under review (Yu *et al.*, 2019).

The CvP calculations are first validated from a comparison against experimental vizualisations of the trefoil-knot vortex dynamics made by Kleckner & Irvine (2013) (not shown). The present numerical setup is also validated against low-Reynolds DNS performed by (Kida & Takaoka, 1987) in terms of the evolution of the global helicity (not shown). In this present contribution we focus on discussing the axial flow and nonlinear dynamics of Kelvin waves generated by the vortex reconnection process are studied.

COHERENT-VORTICITY PRESERVING LARGE-EDDY SIMULATION (CvP-LES)

The compressible, Favre-filtered Navier-Stokes equations are solved using a 6th order compact finite difference scheme solver originally written by Nagarajan *et al.* (2003), under continued development at Purdue University. The solver is based on a staggered grid arrangement, providing superior accuracy compared to a fully collocated approach developed by Lele (1992). The compressible LES formalism introduced by Lesieur *et al.* (2005) is adopted, and the

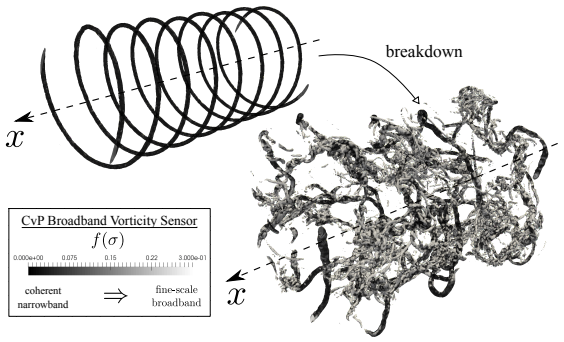

Figure 1. Illustration of CvP turbulence sensor values on helical vortices.

CvP-Smagorinsky closure is considered, which yields accurate results for transitional and high-Reynolds number flows (Chapelier *et al.*, 2018). This approach aims at correcting the eddy-viscosity using a turbulence sensor $f(\sigma)$:

$$\mu_t^{\mathrm{CvP}} = f(\sigma)\mu_t \tag{1}$$

where σ is the ratio of test-filtered to grid-filtered enstrophy, which detects the onset of small scales in the flow with only one additional filtering operation. In particular, the regions in the flow with $\sigma = 1$ will be characterized by a coherent, low-wavenumber motion, while values lower than 1 indicate the presence of small scales (spectral broadening). Fully developed turbulence is characterized by the threshold value σ_{eq}, which is found analytically based on Kolmogorov's model spectrum. The dependency of σ to the degree of spectral broadening in the flow is illustrated in the legend in figure 1. The function $f(\sigma)$ is built such that $f(\sigma = 1) = 0$ and $f(\sigma = \sigma_{eq}) = 1$. This function then modulates the eddy viscosity to reduce the subgrid dissipation in the vicinity of coherent structures. The calibration of σ_{eq} and the shape of the function $f(\sigma)$ are detailed in the work of Chapelier *et al.* (2018).

Validation of the CvP-LES methodology

Taylor-Green Vortex This section features a validation of the present CvP-LES methodology from transitional Taylor-Green vortex computations at $Re = 5000$. The computations are carried out in a periodic box in which large vortices are initialized from analytical velocity and pressure profiles. The CvP-LES results are compared against a DNS computation performed by Chapelier & Lodato (2016), and filtered using a sharp spectral filter with filter width matching the LES grid cutoff. Figure 2 shows the temporal evolution of the volume-averaged, non-dimensional kinetic energy dissipation, and an excellent agreement is found between CvP-LES computations and the filtered DNS for various grid sizes. The results show the capacity of the CvP sensor to deactivate the eddy-viscosity in transitional regions and provide the right amount of subgrid dissipation when reaching the fully-developed turbulent regime, independently of the level of resolution considered.

Transitional Helical Vortices In this section, the CvP-LES methodology is applied to a configuration of temporally developing double helical vortices, which is representative of the wake past rotating devices, such as wind

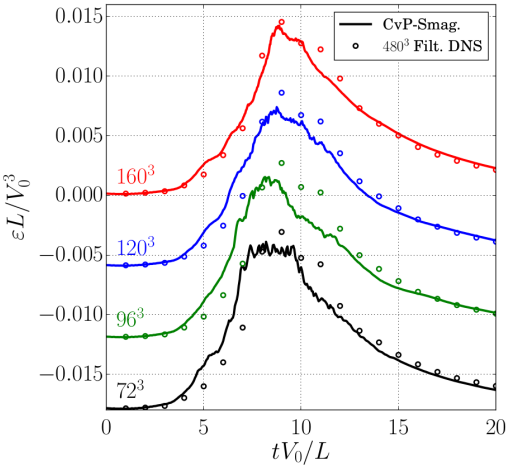

Figure 2. Mesh convergence validation of the CvP-LES methodology from Taylor-Green vortex computations at $Re = 5000$. For the sake of clarity, the LES computations using 72^3, 96^3 and 120^3 grid points are shifted vertically.

turbines or helicopter rotor blades. A parallelepipedic computational domain is considered, with periodic boundary conditions yielding an infinite extent of the helical vortices in the axial direction. The initial velocity field describing the helical vortices is calculated using the Biot-Savart law. This initialization procedure allows for defining arbitrarily the helical pitch h, helical radius R, the vortex-core radius r_c and vortex-core circulation Γ. Additional details about this particular configuration can be found in Chapelier *et al.* (2019). Of particular interest is the ability of the present CvP-LES methodology to capture accurately the growth rates of the helical vortices instability with a minimal number of grid points to represent the vortex core. The growth rates are quantified from the temporal evolution of the helix vortex cores deviation compared to their initial position. CvP-LES simulations are performed, featuring several non-dimensional values of the helical pitch h/R, a Reynolds number based on circulation $Re_\Gamma = 7000$ and a vortex core radius $r_c/h = 0.166$ matching the experimental conditions of Nemes *et al.* (2015). A coarse discretization with 7 grid points per initial vortex cores is considered. To assess the quality of the simulations during the transition of the helical vortices, the evolution of the vortex-core deviation is shown in figure 3. We can see that the growth rates match the experimental results from for various values of the helical pitch. This shows the ability of the present methodology to capture accurately the transient dynamics of topologically complex vortices. In figure 1, we can also see that after the vortex breakdown occurring at then end of the transient period, the CvP sensor activates the subgrid dissipation only where smaller scales are developing, allowing for an accurate representation of the larger vortices dynamics carrying the bulk of the flow kinetic energy.

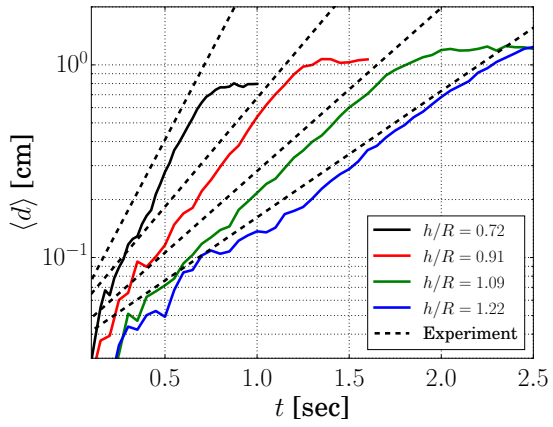

Figure 3. Temporal evolution of the averaged vortex-core deviation in the computational domain from CvP-LES simulations at $Re_\Gamma = 7000$ featuring four different values of the helical pitch h/R (Chapelier *et al.*, 2019). The dashed lines represent the instability growth rates extracted from the experiments of Nemes *et al.* (2015).

CvP-LES OF A TREFOIL VORTEX

Problem Formulation

The trefoil knotted vortex is initialized using a vortex filament, as shown in figure 4, in a periodic, cubic box, defined using the following parametric equation:

$$\begin{aligned} x(\theta) &= R_{min}[\sin(\theta) + 2\sin(2\theta)] \\ y(\theta) &= R_{min}[\cos(\theta) - 2\cos(2\theta)] \\ z(\theta) &= -h\sin(3\theta) \end{aligned} \tag{2}$$

where R_{min} is the minimum radius which is related to the maximal radius in the $x-y$ plane as $R_{max} = 3R_{min}$. The knot radius averaged along the vortex line is $\overline{R} \approx 0.748 R_{max}$. h is a parameter that determines the extent of the knotted vortex in the propagation direction and is selected as $h = R_{min}$. This choice of h has been considered in previous works for the computation of trefoil-knotted vortices, see Kida & Takaoka (1988). The velocity field induced by the vortex filament is determined by integrating numerically the Biot-Savart law:

$$\mathbf{u}(\mathbf{x}) = -\frac{\Gamma}{4\pi}\int K_\nu \frac{(\mathbf{x}-\mathbf{X}(\theta))\times\mathbf{t}(\theta)}{|\mathbf{x}-\mathbf{X}(\theta)|^3} d\theta \tag{3}$$

where $\mathbf{t}(\theta)$ is the tangent vector to the helical filament, with a given circulation Γ and smoothing kernel $K_\nu(r_c)$, a function allowing to define the shape of the vortex core as proposed by Vatistas *et al.* (1991), where r_c is the vortex core radius.

The simulations are performed in a cubic computational domain $\Omega = [0, 15R_{min}]^3$ with periodic boundaries in all directions. Simulations are run with $\overline{R} = 35$ mm, $h = R_{min}$, $\nu = 10^{-6}$ m^2/s. The vortex core radius is chosen as $r_c/\overline{R} = 0.06$ and the Reynolds number based on circulation $Re_\Gamma = 20,000$. These parameters correspond approximately to the conditions in Kleckner & Irvine (2013), where $Re_\Gamma \sim 10000$, $\overline{R} = 45$ mm and $r_c \sim 2$ mm. With 576^3 grid points and 11 points in the initial vortex cores, the flow topology is found to be essentially the same between the simulation (see Yu *et al.* (2018*a*)) and experiment emphasizing the accuracy of the CvP-LES methodology coupled with high-order schemes.

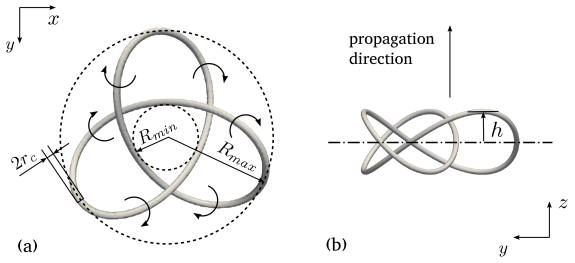

Figure 4. Initial vortex shape defined via the parametric equation 2

Global Flow Evolution

In this section, a physical study of the present flow problem is carried out from a CvP-LES simulation. To track the flow evolution, a non-dimensional time $t^\star = t\Gamma/\overline{R}^2$ is defined. The characteristic evolution stage can be summarized in figure 5. The initial knotted vortex propagates along, and rotates about the z-axis, then gradual distortion and elongation of the vortex filament are observed. This leads to the stretching of the vortex line and reconnection of vortex filaments at three different locations (t= 2.59). After this reconnection event, two distinct vortical structures, initially triangular in shape, are generated and evolve independently from each other. These processes are common among cases with different Reynolds numbers (Yu *et al.*, 2019). While the enstrophy, $\xi = \omega^2/2$, used here to infer the small-scale energy content of the flow, increases with Reynolds numbers as shown in background curves, the flow topology does not show large variations. which is visualized by the large structures. The cascaded reconnection and secondary reconnection occur for high and low Reynolds numbers, respectively after long time simulation as shown in (Yu *et al.*, 2019). The present study focuses mainly on the dynamics of the separated large ring on $Re_\Gamma = 20,000$.

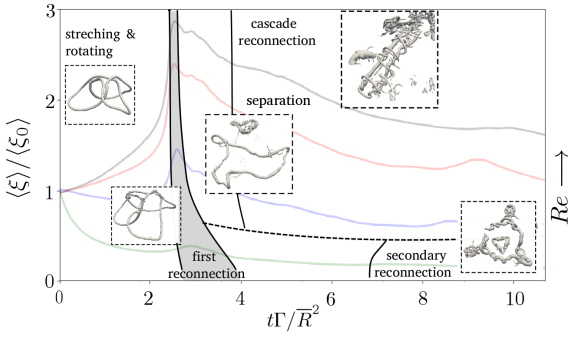

Figure 5. Variation of the flow topology with dimensionless time and Reynolds numbers, indicated in various colors.

Reconnection process generates perturbations on the larger ring which propagate as *Kelvin waves* along the vortex tube, triggering *axial flow*. These Kelvin wave-packets propagate away from the reconnection region, in opposite

directions, and exhibit opposite handedness of helix-shaped structures. The helical structures traveling along each single side of the triangular shaped vortex ring periodically collide with each other, then continue to travel past one another. This process can be clearly seen in figure 7, where the vortex structure is visualized by Q-criterion and colored by helicity density $h = \mathbf{u} \cdot \boldsymbol{\omega}$, so that the red and blue wave packets are propagating towards opposite direction.

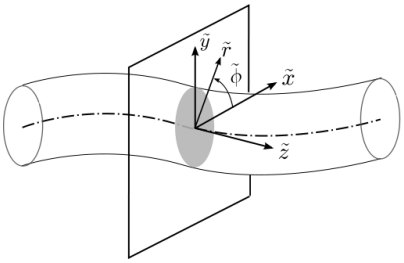

Figure 6. Diagram of local coordinates system along vortex centerline, in cylindrical $(\tilde{r}, \tilde{\phi}, \tilde{z})$

The velocity is extracted along the instantaneous vortex line and projected onto the tangential direction $\tilde{z}$ to obtain the axial velocity $\tilde{w}$. The local coordinate $(\tilde{r}, \tilde{\phi}, \tilde{z})$ and local velocity $\tilde{\mathbf{u}} = \tilde{u}\hat{\mathbf{r}} + \tilde{v}\hat{\boldsymbol{\phi}} + \tilde{w}\hat{\mathbf{z}}$ are defined correspondingly as shown in figure 6. A spectral study is conducted based on the axial flow energy defined as

$$E_{\tilde{w}}(k\ell, t) = \frac{1}{\ell(t)} \int_{\ell} \rho \tilde{w}^2(0,0,\tilde{z},t) e^{-j2\pi k\tilde{z}} d\tilde{z}, \qquad (4)$$

where $\ell(t)$ is the instantaneous length of the large vortex ring. Figures 7, $(a)-(c)$ display the modal energy distribution for axial flow after reconnection on the large vortex ring. The mode $m = 3a$ (a is integer) is always dominant due to the triple symmetry of the structure. After the reconnection, a perturbation in the form of axial flow is excited at the bridge, moving in both directions away from the reconnection region. At $t^* = 3.375$, $m = 6$ dominates corresponding to the well-developed axial flow that travels along the vortex tube. At $t^* = 3.712$, the axial flow collides, yielding a negative interference (axial flow becomes null, the vortex temporarily bursts). After the collision, the axial flow wavepackets propagate past each other and the energy is restored, however with a modification in the energy distribution over modes, with less energetic lower modes and more energetic higher modes, i.e. higher wavenumbers.

Kelvin Waves Propagation

The current LES shows that the wave packets propagating in the opposite direction collide and pass by, similar to the linear wave propagation. After multiple collision cycles, higher order axial modes get generated and distributed in different location along the vortex rings (see figure 8), which implies the existence of a dispersive behavior. To quantify the dispersion relationship, the oscillation pattern for each mode is studied (figure 9), and the characteristic oscillation frequency (f) is determined correspondingly. The collision of wave packets at $t\Gamma/R^2 \sim 3.7$ results in a nullification of energy for dominant modes, which can also be observed in figure 9, where a rapid decrease occurs during

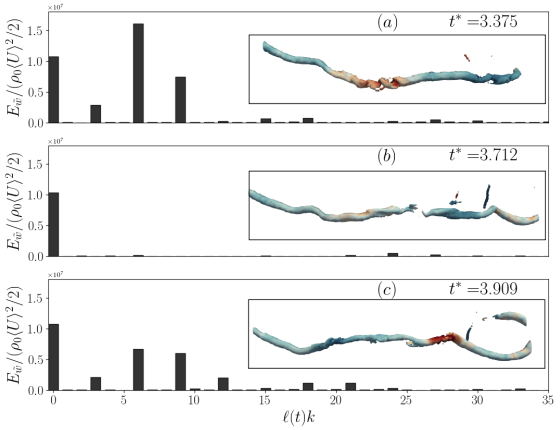

Figure 7. Oscillation frequencies and wavenumbers show linear relationship.

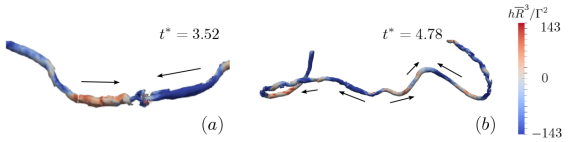

Figure 8. (a) The first collision of kelvin waves in the form of compact wave packets; (b) after 3-4 collisions, the wave component distribute uniformly on the vortex loop.

the collision, modifying the original oscillation pattern of each mode. Such modification effect is more apparent for lower wavenumbers ($k\ell = 1-5$).

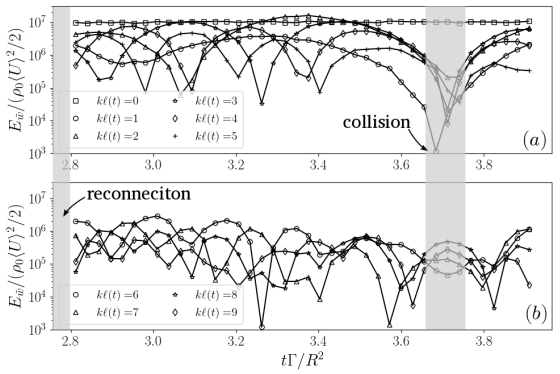

Figure 9. Then axial component energy along centerline oscillate with characteristic frequency for first then axial modes after reconnection ($t\Gamma/R^2 \sim 2.5$); (a) $k\ell = 0-5$; (b) $k\ell = 6-7$

The group velocity v_g and phase velocity v_p can be determined from dispersion relation shown in figure 10 as

$$v_g = \frac{df}{dk}, \quad v_p = \frac{f}{k}. \qquad (5)$$

In the current simulations, $v_g \approx v_p$, which shows that minimal dispersion is captured during the propagation of the Kelvin wave packets. As shown in figure 8 (b), after multiple collisions, the axial flow wave packets spread into mul-

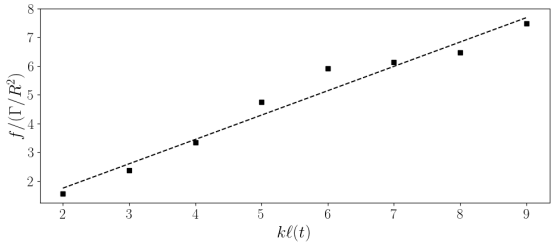

Figure 10. Oscillation frequencies and wavenumbers show linear relationship.

tiple wave packets, indicated by alternating direction of the axial flow. Such phenomenon suggests the separation of the higher wavenumbers along the vortex tube indicating dispersion. Moreover, the presence of higher modes of axial flow also indicates the nonlinear nature of the perturbations generated upon reconnection. With higher spatio-temporal resolution, the dispersion can be better quantified in the simulations.

Centerline and Tube-based Energy

The centerline axial energy oscillation shown in figure 9 indicates that the energy is either redistributed into the normal direction, or away from the centerline. To study this, we study the evolution of total kinetic energy and the axial kinetic energy at the centerline, defined as,

$$E_{a,c} = \frac{1}{2}\int_{\ell(t)} \rho \tilde{w}^2 d\tilde{z},$$
$$E_{tot,c} = \frac{1}{2}\int_{\ell(t)} \rho(\tilde{u}^2+\tilde{v}^2+\tilde{w}^2) d\tilde{z}, \tag{6}$$

where $\ell(t)$ denotes the instantaneous length of the whole knotted structure before reconnection, and only that of the larger ring after reconnection. On the centerline, the axial

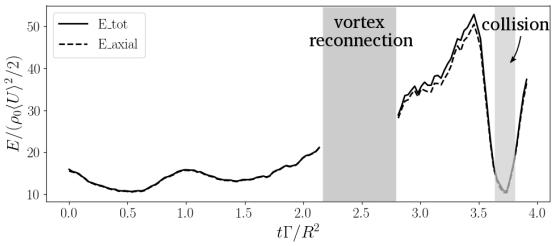

Figure 11. Total kinematic energy $E_{tot,c}$ (solid line) and the component along axial direction $E_{a,c}$ (dashed line) on vortex centerline. After reconnection, only energy of large ring are shown.

component of the velocity dominates before and after the reconnection. After reconnection, the kinetic energy is redistributed in the normal directions shown by the difference between the curves shown in figures 11. Moreover, after the collision of axial flow modes, both the total energy and the axial energy along the centerline rapidly drop indicating the energy outflow from the centerline. This can also be realized in the visualization of "hollow structures" formed upon collision, as shown in figure 12. To visualize the hollow structure, lower value of Q-isosurface is chosen in comparison to the one chosen in figure $7(b)$ (which is at the same time instant).

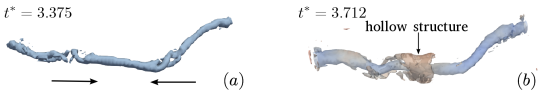

Figure 12. Formation of hollow structure when two wave packets colliding.

The axial flow collision does not cause abrupt changes in the global energy as shown previously by Yu *et al.* (2018*a*). However, the variation of total kinetic energy within the vortex tube can be used to determine the variation of transverse velocity within the tube. To this end, we define the total kinetic energy and the axial kinetic energy inside the vortex tube as,

$$E_{a,tube} = \frac{1}{2}\iiint_{\Omega} \rho \tilde{w}^2 d\Omega,$$
$$E_{tot,tube} = \frac{1}{2}\iiint_{\Omega} \rho(\tilde{u}^2+\tilde{v}^2+\tilde{w}^2) d\Omega, \tag{7}$$

where Ω denotes the vortex tube volume of whole knotted structure before reconnection, and only that of the large separated ring after reconnection. Volume Ω has a boundary defined as the location of vorticity magnitude $|\boldsymbol{\omega}| = 0.05|\boldsymbol{\omega}|_{axial}$ on each normal plane.

Before reconnection, the total energy increases faster than the axial component, so that the vortex stretching results in more energy on rotation than axial motion. After reconnection, the total kinetic energy within the tube is almost invariant, as shown in figure 13 (solid line). Moreover, the axial kinetic energy shows gradual increase after reconnection before the collision of the axial flow components, indicating velocity generated in axial direction due to the perturbations from reconnection. Upon collision of the axial flow, the total energy inside the tube remains almost invariant, however the total axial energy decreases, indicating redistribution of energy in transverse velocity components. This also highlights the local nature of the axial flow collision within the tube. Even though the centerline and total axial energy get cancelled during the collision, the total energy does not vary due to the redistribution of velocity to the components normal to the vortex tube.

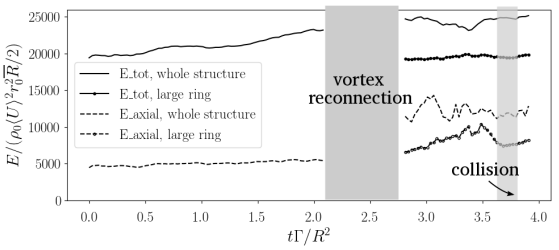

Figure 13. Total kinematic energy $E_{tot,tube}$(solid line) and the component along axial direction $E_{a,tube}$(dashed line) integrated in vortex tube.

CONCLUSION

Simulation of the vortex reconnection occurring in trefoil-knotted vortices configuration has been carried-out using a novel methodology for Large-Eddy Simulation, named Coherent-vorticity Preserving (CvP). The ability of the CvP turbulence sensor to sort the large, coherent scales from the small, chaotic structures has been assessed from visualizations of the Q-criterion colored by the values of the sensor.

This methodology is found to be successful as well for the quantitative prediction of various other flow configurations. CvP-LES simulations of the Taylor-Green vortex at Reynolds $Re = 5000$ highlighted the ability of the methodology to accurately describe the transition and subsequent fully-developed regime considering various grid resolutions. Accurate instability growth rates have also been obtained in the context of temporally-developing double helical vortices with coarse grids featuring a minimal number of grid points for discretizing the initial vortex cores.

In present sutdy, a study of high-Reynolds number vortex reconnection mechanisms and Kelvin waves propagation has been carried out from Cvp-LES computations of trefoil knotted vortices. The numerical simulation of the trefoil knotted vortex shape shows a vortex filament entanglement process in three locations of the main structure leading to the separation of this structure in two distinct vortices.Such reconnection results in large perturbations that excites the Kelvin waves coupled with axial flow propagating along both separated vortex rings.

The present study focused on such wave packets propagating on the large vortex ring, in the form of opposite handedness helical structures, which travel along the vortex loop, collide, and pass by each other. The spectral study based on the axial flow energy reveals the cancellation of most modes during the collision and the independent oscillation of each mode before collision.

The evaluation of the characteristic oscillation frequency shows minimal dispersion captured by the current LES methodology. The small amount of dispersion captured in the simulations only causes the spreading of wave packets after several collision cycles. Improved estimates of the dispersion relations for the Kelvin waves can be obtained using higher resolution simulations.

The axial velocity dominates on the center line during the evolution, except during the collision, when the energy leaves the centerline, as well as the axial velocity component. Such transer is highly local and also required DNS resolution for more quantitative analysis.

ACKNOWLEDGMENTS

The authors acknowledge the support of the Army Research Office's Young Investigator Program (ARO-YIP) Award W911NF-18-1-0045 for the proposal entitled *Coherent-vorticity-Preserving (CvP) Large-Eddy Simulation (LES) of Very-High-Reynolds-Number Vortex Dynamics* and the inspiring conversation with Dr. Matthew Munson (Army Research Office).

REFERENCES

Chapelier, J-B & Lodato, Guido 2016 A spectral-element dynamic model for the large-eddy simulation of turbulent flows. *J. Comput. Phys.* **321**, 279–302.

Chapelier, J.-B., Wasistho, B. & Scalo, C. 2018 A coherent vorticity preserving eddy-viscosity correction for large-eddy simulation. *J. Comput. Phys.* **359**, 164–182.

Chapelier, J.-B., Wasistho, B. & Scalo, C. 2019 Large-eddy simulation of temporally developing double helical vortices. *Journal of Fluid Mechanics* **863**, 79113.

Hussain, A. K. M. Fazle 1986 Coherent structures and turbulence. *J. Fluid Mech.* **173**, 303–356.

Kida, S. & Takaoka, M. 1987 Bridging in vortex reconnection. *The Physics of Fluids* **30** (10), 2911–2914.

Kida, S. & Takaoka, M. 1988 Reconnection of vortex tubes. *Fluid Dynamics Research* **3**, 257–261.

Kimura, Yoshifumi & Moffatt, Keith 2014 Reconnection of skewed vortices. *J. Fluid Mech.* **751**, 329–345.

Kleckner, D. & Irvine, W. T. M. 2013 Creation and dynamics of knotted vortices. *Nature physics* **9** (4), 253–258.

Lele, S.K. 1992 Compact finite difference schemes with spectral-like resolution. *J. Comput. Phys.* **103** (1), 16–42.

Lesieur, M., Métais, O. & Comte, P. 2005 *Large-Eddy simulations of turbulence*. Cambridge University Press.

Nagarajan, S., Lele, S.K. & Ferziger, J.H. 2003 A robust high-order compact method for large eddy simulation. *J. Comput. Phys.* **191**, 392–419.

Nemes, A., Lo Jacono, D., Blackburn, H. M. & Sheridan, J. 2015 Mutual inductance of two helical vortices. *J. Fluid Mech.* **774**, 298–310.

Scheeler, M. W., Kleckner, D., Proment, D., Kindlmann, G. L. & Irvine, W. T. M. 2014 Helicity conservation by flow across scales in reconnecting vortex links and knots. *Proc. Natl. Acad. Sci.* **111** (43), 15350–15355.

Spalart, Philippe R. 1998 Airplane trailing vortices. *Annual Review of Fluid Mechanics* **30** (1), 107–138.

Vatistas, G. H., Kozel, V. & Mih, W. C. 1991 A simpler model for concentrated vortices. *Exp. Fluids* **11** (1), 73–76.

Yu, Z., Chapelier, J.-B. & Scalo, C. 2018*a* Coherent-vorticity preserving large-eddy simulation of trefoil knotted vortices. *2018 AIAA Aerospace Sciences Meeting* .

Yu, Z., Chapelier, J.-B. & Scalo, C. 2018*b* Coherent-vorticity preserving large-eddy simulation of vortex rings under large perturbations. *2018 AIAA Fluid Dynamics Conference* .

Yu, Z., Chapelier, J.-B. & Scalo, C. 2019 Large-eddy simulation of trefoil knotted vortices. *submitted to Journal of Fluid Mechanics* .